Letter

Quantum sensing of magnetic fields with molecular color centers

Kathleen R. Mullin,[1] Daniel W. Laorenza,[2] Danna E. Freedman,[2] and James M. Rondinelli[1,*]

[1]Department of Materials Science and Engineering, Northwestern University, Evanston, Illinois 60208, USA

[2]Department of Chemistry, Massachusetts Institute of Technology, Cambridge, Massachusetts 02139, USA

(Received 7 February 2023; revised 13 June 2023; accepted 10 October 2023; published 8 November 2023)

Molecular color centers, such as $S = 1$ Cr(o-tolyl)$_4$, show promise as an adaptable platform for magnetic quantum sensing. Their intrinsically small size, i.e., 1–2 nm, enables them to sense fields at short distances and in various geometries. This feature, in conjunction with tunable optical read-out of spin information, offers the potential for molecular color centers to be a paradigm shifting materials class beyond diamond-NV centers by accessing a distance scale opaque to NVs. This capability could, for example, address ambiguity in the reported magnetic fields arising from two-dimensional magnets by allowing for a single sensing technique to be used over a wider range of distances. Yet, so far, these abilities have only been hypothesized with theoretical validation absent. We show through simulation that Cr(o-tolyl)$_4$ can spatially resolve proximity-exchange versus direct magnetic-field effects from monolayer CrI_3 by quantifying how these interactions impact the excited states of the molecule. At short distances, proximity exchange dominates through molecule-substrate interactions, but at further distances the molecule behaves as a typical magnetic sensor, with magnetostatic effects dominating changes to the energy of the excited state. Our models effectively demonstrate how a molecular color center could be used to measure the magnetic field of a two-dimensional magnet and the role different distance-dependent interactions contribute to the measured field.

DOI: 10.1103/PhysRevResearch.5.L042023

I. Introduction. Precise measurements of magnetic fields are an important tool in understanding the spin properties and spatial distribution of magnetic fields in low-dimensional materials. Over the past decade, intensive technique development in magnetic-field sensing showcased the importance of coupling spatial resolution with minute sensitivity [1–3]. Where techniques, such as fluxgate [4] and Hall-effect sensors [5,6], are limited to micrometer-scale sensing resolution, recent advances in quantum sensing have focused on optically detected magnetic resonance (ODMR) with color centers in semiconductors, e.g., diamond-NV centers [7,8]. These defect-based color centers feature two key advantages—optical read-out and a high sensitivity to local magnetic fields. In ODMR, the ground-state spin is initialized with optical excitation, probed with microwave pulses to coherently drive the magnetic sublevels of a triplet ground state via a singlet excited state and then optical read-out is used to determine the populations of the spin sublevels [7]. These color centers allow for nanoscale resolution of magnetic fields [9], but do not allow for intimate sensing of fields near the analyte. Defect qubits, like diamond-NV centers, are spatially limited. They are difficult to bring in close proximity to the analyte as the defect is embedded in a crystal [10], e.g., the smallest analyte-qubit distance reported is 9 nm [11]. This limitation is functionally related to the nature of these defects, many of which would not be thermodynamically stable in isolation; furthermore, placing defects closer to the surface leads to their removal or lower coherence times.

Molecules are zero dimensional and functionally all surface. They may feature lower coherence times, but they are tunable and solution processable. This portability, in particular, enables postsynthetic processing of molecular color centers (MCCs) in thin-film geometries to probe magnetic fields with distances ranging from angstroms to micrometers. Recent work has even highlighted this functionality with self-assembled monolayers of radical-based spins [12]. The MCC Cr(o-tolyl)$_4$ has a paramagnetic triplet $S = 1$ ground state (^{3}A symmetry[1]) owing to the Cr^{4+} center and a zero-field splitting that allows for optical addressability analogous to color centers in solids [13–16]. Here, light is used to resonantly excite an electron between the $M_s = 0, \pm 1$ sublevels via a singlet excited state [7,17]. When exposed to even tiny magnetic fields, these electronic states undergo a Zeeman shift in energy (E') proportional to the intensity of the magnetic field (B), the free-electron g actor (g_e), and the Bohr magneton (μ_B) with S dimensionless as $E' = g_e \mu_B S B$. Here E' is the difference in energy of the first singlet excited state (^{1}E symmetry) in the presence of a finite magnetic field ($E_{B,^1\mathrm{E,unrel}}$) to that at zero

*jrondinelli@northwestern.edu

Published by the American Physical Society under the terms of the Creative Commons Attribution 4.0 International license. Further distribution of this work must maintain attribution to the author(s) and the published article's title, journal citation, and DOI.

[1]While the isolated molecule has C_1 symmetry, we use the symmetry labels of the idealized tetrahedral structure.

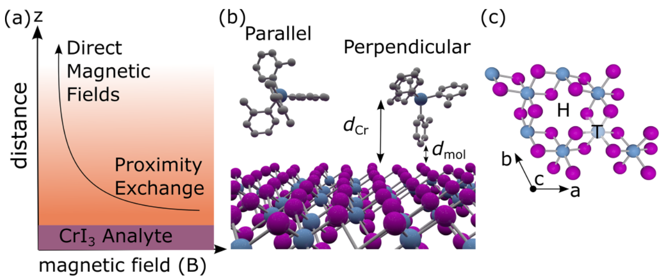

FIG. 1. (a) Sensor-analyte schema to probe magnetic interactions by changing the distance between the MCC sensor and analyte. Cr(o-tolyl)$_4$ on CrI_3 can (b) adopt two configurations with an o-tolyl group parallel or perpendicular to the surface at the (c) hollow (H) and top (T) Cr sites on monolayer CrI_3.

field ($E_{B=0,{}^1\mathrm{E},\mathrm{rel}}$):

$$E' = E_{B,{}^1\mathrm{E},\mathrm{unrel}} - E_{B=0,{}^1\mathrm{E},\mathrm{rel}}. \quad (1)$$

Although magnetic-field sensing is obtained experimentally by measuring shifts in the energy levels $M_s = 0, \pm 1$ sublevels [18], we use shifts in the ^{1}E excited state as a surrogate in our model.[2]

Recently, many correlated two-dimensional (2D) magnets such as ferromagnetic $CrGeTe_3$ and antiferromagnetic CrI_3, which exhibits layer-dependent magnetic ordering below 45 K, have been studied [20,21]. To fully characterize these materials, high-resolution sensors are needed. CrI_3 is an ideal analyte for quantum magnetic-field sensing at the nanoscale, as prior studies have shown large discrepancies (five orders of magnitude) in magnetic fields with distance away from the surface of the monolayer [Fig. 1(a)]. Zhong *et al.* used a CrI_3/WSe_2 heterostructure to calculate an effective magnetic field of 13 T from the valley splitting in WSe_2 at 3.50 Å from CrI_3. Single spin microscopy with a diamond-NV center has measured maximum magnetic fields of 0.31 mT at a distance of 62 nm from CrI_3 [22,23]. Additional studies on CrI_3-based heterostructures have shown that such large magnetic fields are due to proximity exchange rather than the typical magnetostatics associated with stray magnetic fields [24,25]. This raises the question of how the 2D magnet distributes the magnetic flux, and this knowledge is needed to guide co-design of spin-based logic and memory devices [26].

One approach to resolve the distance dependent magnetic-field strengths is to layer thin films of Cr(o-tolyl)$_4$, the sensor, of varying thicknesses on CrI_3, the analyte and perform thickness dependent ODMR measurements. This quantum sensing geometry in the single-molecule limit is shown in Fig. 1(a) and it is the configuration we consider. (We discuss thin-film effects later.) We expect two important magnetic interactions, proximity exchange and direct magnetic fields, to occur between Cr(o-tolyl)$_4$ and the CrI_3 substrate. Proximity exchange is a local effect and should dominate at short distances d where electron wave functions directly overlap [27]; in contrast, direct magnetic fields from dipolar contributions should dominate at longer distances. Notably, it is very difficult to measure proximity exchange through conventional magnetic sensing techniques outside of NMR spectroscopy. Here, we use density-functional theory (DFT) simulations with magnetostatic calculations to show how the first-excited state of Cr(o-tolyl)$_4$ is affected by these interactions as a function of distance, demonstrating MCC as a quantum magnetic sensing platform.

II. Computational methods.

a. Density-functional theory simulations. Ab initio calculations were performed using the Vienna *ab initio* Simulation Package (VASP version 5.4.4) [28–31] using projector augmented wave pseudopotentials [32,33] and the PBE exchange correlation functional [34,35] with the following valence configurations: I($5s^2 5p^5$), Cr($3d^5 4s^1$), C($2s^2 2p^2$), and H($1s^1$). We used a 600 eV energy cutoff for the plane wave expansion and an energy convergence of 1×10^{-7}. For k-point integrations, Gaussian smearing of 0.05 eV was used.

For all systems involving the isolated molecule and the molecule on the substrate a single k point at the Γ point was used. For calculations on the 2D monolayer CrI_3, a $9 \times 9 \times 1$ k-point grid was used. All components of the system were initially relaxed with a force convergence of 10^{-3} meV/Å within in a simulation cell providing a spacing of 15 Å between periodic images of the molecule in all directions or the substrate in the out of plane direction. Excited-state (es) calculations were performed using the Δ-SCF method [36,37]. We calculate $E_{es}^{\uparrow\downarrow}$ by subtracting the total energy of a constrained occupancy calculation, where the electron in the spin-up highest-occupied molecular orbital (HOMO) is promoted to the spin-down lowest-unoccupied molecular orbital (LUMO) from a standard ground-state DFT calculation. For all calculations, including the constrained occupancy calculations, the relaxed ground-state geometry is used. Changes in $E_{es}^{\uparrow\downarrow}$ were then used to calculate the implied magnetic fields based on the Zeeman shift using Eq. (1).

b. Magnetic-field calculations. We modeled a freely suspended monolayer flake of CrI_3 with in-plane dimensions of 1×1 μm^2 within a vacuum inside a 2×2 μm^2 area simulation cell. Grid-based direct magnetic-field calculations were performed by tessellating the spin density of monolayer CrI_3 to fit a 1×1 μm^2 array. Every element in the spin-density grid was treated as its own magnetic block, with the normalized spin density as the magnetic polarization in the z direction, J_z. Previous literature has shown that CrI_3 is strongly magnetically polarized in the z direction [23]. To be consistent with these results, we used the spin polarization from a collinear calculation and assigned it to the z direction. For constant polarization calculations, the 1×1 μm^2 flake of CrI_3 was treated as a single block with J_z determined from our DFT calculations. The equations below were used to calculate the magnetic field for both models from the polarization (J_z), the position of the magnetic block (x, y, z), and the position at

[2]Accurate quantitative changes in zero-field splitting values are difficult to obtain with single-particle orbitals from DFT [19]. Post-Hartree-Fock methods (i.e., complete active space self-consistent field methods) give more accurate results but are not tractable for the sensor-analyte system explored. This necessitates a surrogate value for zero-field splitting. Here we use the ^{1}E singlet excited state that is involved in the excitation to the magnetic sublevels as a proxy.

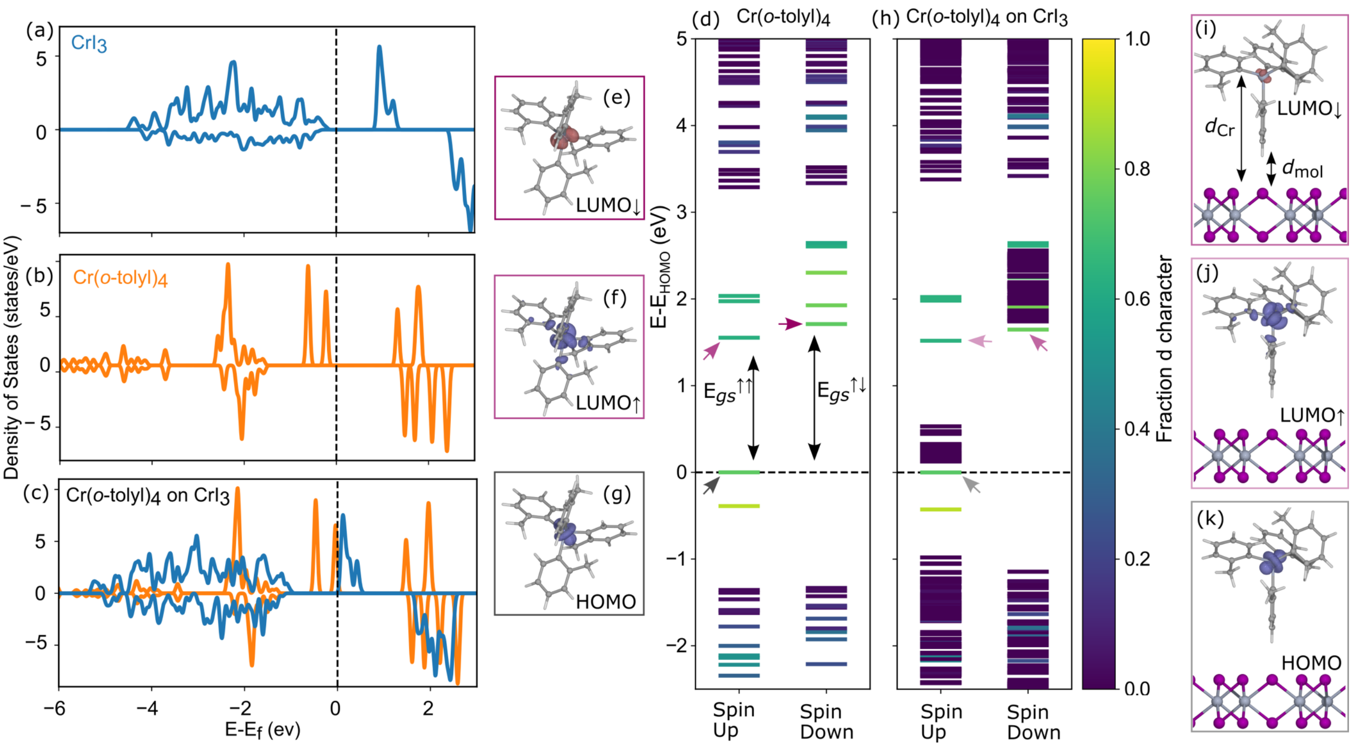

FIG. 2. Electronic density of states (DOS) plots for (a) monolayer CrI_3, (b) Cr(*o*-tolyl)$_4$, and (c) Cr(*o*-tolyl)$_4$ adsorbed on the CrI_3 surface (perpendicular geometry at the hollow site, see Fig. 1). Quantitative molecular-orbital diagrams highlighting the d-orbital character of (d) Cr(*o*-tolyl)$_4$ and (h) Cr(*o*-tolyl)$_4$ adsorbed on monolayer CrI_3. Panels (e)–(g) and (i)–(k) show visualizations of selected molecular orbitals for the isolated molecule and the molecule adsorbed on CrI_3, respectively, at $d_{\mathrm{mol}} = 3$ Å ($d_{\mathrm{Cr}} = 9$ Å).

which the magnetic field was calculated (x_i, y_i, z_i):

$$B_x(x, y, z) = \frac{J_z\mu_0}{4\pi}\sum_{i=1}^{2}\sum_{j=1}^{2}\sum_{k=1}^{2}\tan^{-1}\left(\frac{(y-y_i)(z-z_i)}{(x-x_i)\sqrt{(x-x_i)^2+(y-y_i)^2+(z-z_i)^2}}\right)(-1)^{i+j+k}, \tag{2}$$

$$B_y(x, y, z) = \frac{J_z\mu_0}{4\pi}\sum_{i=1}^{2}\sum_{j=1}^{2}\sum_{k=1}^{2}-\ln\left((z-z_k)\sqrt{(x-x_i)^2+(y-y_i)^2+(z-z_i)^2}\right)(-1)^{i+j+k}, \tag{3}$$

$$B_z(x, y, z) = \frac{J_z\mu_0}{4\pi}\sum_{i=1}^{2}\sum_{j=1}^{2}\sum_{k=1}^{2}-\ln\left((y-y_i)\sqrt{(x-x_i)^2+(y-y_i)^2+(z-z_i)^2}\right)(-1)^{i+j+k}. \tag{4}$$

For the grid-based approach, the impact of each magnetic block on each cell in the array for the magnetic field was calculated via Eqs. (2)–(4) and then summed to produce the final calculated magnetic field. To increase the efficiency of the calculations, the periodic nature of the magnetic surface was exploited using Boolean operations to minimize the number calculations. Specifically, the equation employed for calculating the field has four parameters that vary based on the location in the final magnetic field and the location in the substrate, $x - x_i$, $y - y_i$, $z - z_i$, and J_z. If all these parameters are equivalent between two cells, then the contribution to the final magnetic field is the same. We made use of these equivalencies to calculate only the unique combinations of the parameters and then assign the results to the appropriate locations in the final grid.

The above approach results in a vector magnetic field that can be calculated at any point outside the simulation cell. However, when this field is sensed using a molecule, a scalar value will be read as the field will be quantized along the magnetization axis for the molecule. To include the effects of the magnetization axis in our results, we perform a scalar projection of the magnetic field vector (**B**) along the unit vector for the magnetization axis (**M**), i.e., $B = \mathbf{B} \cdot \mathbf{M}$. The projection can be performed for any arbitrary axis. Results from this grid based and the average spin-density models quantitatively agree at distances >20 Å (Fig. 5).

III. Results and discussion.

a. Proximity exchange interactions. We first performed electronic structure calculations on monolayer CrI_3 at the DFT-PBE level without spin-orbit coupling and in a ferromagnetic spin configuration. Figure 2(a) shows there is a 1.1 eV band gap and a large spin polarization, which leads to a local spin moment of 3.3 μ_B on the Cr^{3+} site consistent with prior monolayer studies [38]. Next, we simulated the electronic structure of Cr(*o*-tolyl)$_4$ which has the ^{3}A ground state (*gs*) with both the d_{z^2} and $d_{x^2-y^2}$ orbitals singly occupied [Fig. 2(b)]. The first ^{1}E excited state involves a spin nonconserving transition to a doubly occupied $d_{x^2-y^2}$ orbital. Figure 2(d) shows that the highest occupied molecular orbital (HOMO), spin-up lowest unoccupied molecular orbital (LUMO), and spin-down LUMO have significant *d* character [Figs. 2(e)–2(g)]. The energy difference between the HOMO and LUMO ($E_{gs}^{\uparrow\uparrow}$) is 1.52 eV, while the energy difference between the spin-up HOMO and the spin-down LUMO ($E_{gs}^{\uparrow\downarrow}$) is 1.64 eV. We find in the gas-phase approximation that the excited-state energy is 0.62 eV, which is underpredicted from recent experiments that approximate it as 1.21 eV [14]. This underestimation is expected based on our use of a semilocal density functional.

Next, we created the combined analyte-sensor system. Cr(*o*-tolyl)$_4$ is brought in proximity to the CrI_3 surface in a parallel and perpendicular configuration [Fig. 1(b)]. With these two configurations, we carried out adsorption site calculations with the metal center in Cr(*o*-tolyl)$_4$ in the hollow and top positions of CrI_3 [Fig. 1(c)], which included van der Waals energy corrections implemented with the DFT-D3 method of Grimme [39,40]. The lowest-energy configuration is the perpendicular orientation of the molecule at the hollow adsorption site at a distance of $d_{\mathrm{mol}} \approx 2.7$ Å ($d_{\mathrm{Cr}} \approx 10$ Å) from the surface. These two distances, shown in Fig. 1(b), give the distance between the surface atom in monolayer CrI_3 that is most extended in the out-of-plane direction d_z, with the nearest atom or the Cr cation, respectively, in Cr(*o*-tolyl)$_4$. The energies for other sites were similar with a 40 μeV difference between the lowest- and highest-energy configurations (see Appendix B). (Our calculations assume a ferromagnetic ordering between the molecule and the substrate. An antiferromagnetic ordering was found to be equally as stable with a change in energy lower than our 1×10^{-7} convergence threshold.)

Figure 2(c) shows that the electronic structure of the constituent materials in the combined system is largely unchanged in the equilibrium geometry. There is a rigid shift in CrI_3 states, owing to surface Fermi-level pinning (charge neutrality level), which brings the Cr(*o*-tolyl)$_4$ HOMO just below the CrI_3 conduction band. The semiconducting nature of monolayer CrI_3 persists with minor changes in bandwidth. Similarly, there is a minor increase in the width of the HOMO. Figure 2(h) presents the fraction *d* orbital character for Cr(*o*-tolyl)$_4$ on CrI_3 in its equilibrium position. Figures 2(i)–2(k) show no significant change in character for the orbitals in the Cr(*o*-tolyl)$_4$ molecule. These findings indicate that Cr(*o*-tolyl)$_4$ is physisorbed onto CrI_3. (The parallel geometry also leads to no noticeable changes in the electronic structure of the system.)

In the aforementioned equilibrium geometry, we find that $E_{gs}^{\uparrow\uparrow}$ and $E_{gs}^{\uparrow\downarrow}$ increase slightly to 1.55 and 1.71 eV, respectively. $E_{es}^{\uparrow\downarrow}$ also changes to 0.540 eV. Additionally, we calculated the excited-state energy of the molecule in the as-adsorbed geometry without the substrate and found it to be 0.537 eV. We use these changes in the ^{1}E excited-state energy of Cr(*o*-tolyl)$_4$ adsorbed on CrI_3 compared with the adsorbed Cr(*o*-tolyl)$_4$ without the substrate to calculate the implied magnetic field sensed by the molecular color center through the Zeeman interaction. We use the as-adsorbed, lower excited-state energy as a comparison to the distance dependent excited-state energies to calculate the lower bound of the magnetic field without any contributions from structural distortions. Here we obtain $B = 94$ mT at the equilibrium distance of 3 Å. We next examined the changes to these energies as a function of distance between between Cr(*o*-tolyl)$_4$ and CrI_3 as means to map the magnetic-field distribution transverse to the analyte. Figure 3(a) shows that the energy of the first-excited state decreases as Cr(*o*-tolyl)$_4$ approaches CrI_3 over the range 2.7 Å $\leqslant d_{\mathrm{mol}} \leqslant$ 10 Å. This value falls off cubically as the distance increases, as shown in Fig. 3(b), with the smallest computed field being 5.0 mT at 10 Å. As with the isolated molecule, these calculations do not account for relaxations in the excited state. The excited-state energies in the combined system are obtained relative to the structure of the relaxed molecule at the equilibrium distance without any geometric changes due to the change in distance from CrI_3; therefore, they represent the smallest changes expected as atomic displacements would further increase the energy differences.

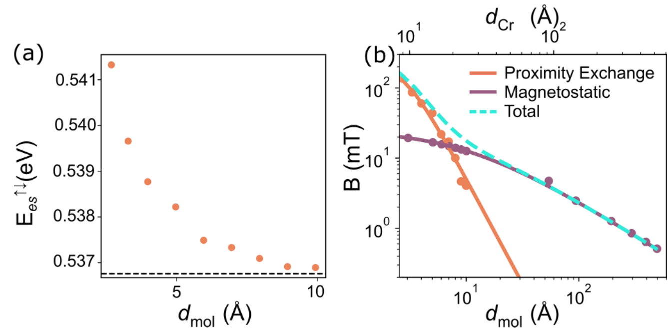

FIG. 3. (a) Distance-dependent energies of the ^{1}E excited state ($E_{es}^{\uparrow\downarrow}$) of Cr(*o*-tolyl)$_4$ near CrI_3. The horizontal broken line shows $E_{es}^{\uparrow\downarrow}$ for the isolated molecule. (b) Total distance-dependent magnetic fields from CrI_3 and contributions to the field from proximity exchange and magnetostatic contributions. Direct magnetic fields are quantized along the easy axis of Cr(*o*-tolyl)$_4$ (see text).

We find the excited-state energy of the isolated molecule changes from 0.621 eV in the fully relaxed geometry to 0.537 eV when the molecule's geometry is taken from the relaxed equilibrium combined structure. We use E' from the fully relaxed molecule to calculate an effective magnetic field of $B = 2.24$ T at $d_{\mathrm{mol}} = 2.7$ Å from the surface. This may be compared with $B = 140$ mT obtained at the same distance using $E_{B=0,^1E}$ from an unrelaxed, as adsorbed geometry. This discrepancy is due to steric distortions to the inner shell of the Cr(*o*-tolyl)$_4$ when adsorbed on the CrI_3 surface without charge transfer or bond formation. We find a change in the coordination environment leading to an increase in the τ_4' geometry index, which quantifies the distortion of a four-coordinate metal complex on a scale from zero (square planar) to one (tetrahedral) [41], from 0.941 to 0.960 for the isolated molecule and the molecule on the surface, respectively. As this change is caused by the interaction of the molecule with the surface, we expect it to decrease with increasing distance between the molecule and the substrate. Raman or infrared

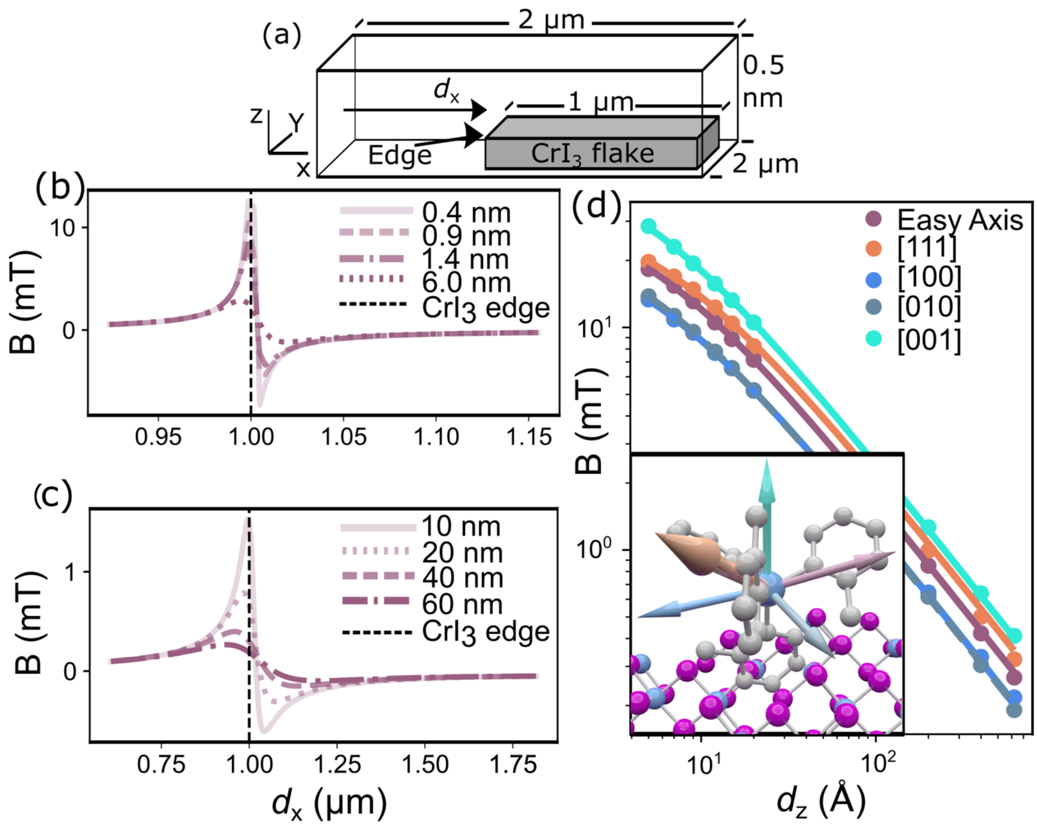

FIG. 4. (a) Schematic of the simulation cell for the magnetostatic models. (b), (c) Computed magnetic fields from CrI_3 at variable d_z values. All results use the linear trajectory shown in panel (a) and are projected along the easy axis of Cr(o-tolyl)$_4$. The broken vertical line indicates the edge of the monolayer. (d) Easy-axis orientation effects on the magnetostatic component of the sensed B field. (inset) Vectors corresponding to orientations of the easy axis used. All vectors are projected onto the geometry of Cr(o-tolyl)$_4$ molecule adsorbed on CrI_3.

spectroscopy could be used to observe the structural distortion through shifts in the vibrational mode frequencies [42].

b. Magnetostatic interactions. Here, we modeled a freely suspended monolayer flake of CrI_3 with in-plane dimensions of 1×1 μm^2 within vacuum inside a 2×2 μm^2 area simulation cell in order to sample the field at the edge and above the flake [Fig. 4(a)]. The magnetic field was sampled every 7 Å over the plane of the simulation cell at vertical distances from the flake between 5 Å $\leqslant d_z \leqslant$ 600 Å. For input into the magnetostatic simulation, we modeled the magnetic polarization of CrI_3 using two methods: (1) a constant polarization calculated from an average of the DFT calculated spin density and (2) a full spin-density with each element in the spin-density grid treated as a magnetic parallelepiped. We used the grid-based spin-density approach (model 2) to calculate magnetic fields at distances less than 20 Å, while for greater distances we used the average calculated spin density (model 1). Numerical details and information on quantitatively agreement are described in the methods section. The largest differences in magnetic fields from these two models occur for short distances, e.g., the difference in maximum field is 4.6 mT at 5 Å. This difference is much smaller than the five orders of magnitude discrepancy between previous experimental measurements.

Figures 4(b) and 4(c) show that the magnetic field sharply increases in magnitude at the edge of the CrI_3 surface and then decreases to a small value over the top of the surface. The field then rapidly decreases to zero in the lateral direction beyond the CrI_3 boundary. Figures 4(b) and 4(c) further show that the peak magnetic-field amplitude along the normal direction d_z of monolayer CrI_3 increases and becomes more localized (decreasing peak width) with decreasing distance between Cr(o-tolyl)$_4$ and the analyte. For $d_z = 60$ nm, we find the magnetic field $B = 0.28$ mT.

Previous continuous-wave optically detected magnetic resonance (cw-ODMR) measurements with the molecular color center, Cr(o-tolyl)$_4$ diluted in a single crystalline host of Sn(o-tolyl)$_4$, have illustrated that external magnetic fields $\geqslant$1 mT are readily measurable [13]. However, since these measurements were performed on ensembles of Cr^{4+} ions, we cannot directly determine a precise magnetic-field sensitivity of individual Cr^{4+} ions. Instead, we can estimate the upper bound on sensitivity for cw-ODMR and pulsed ODMR experiments given by Eqs. (5) and (6), respectively [43]. The magnetic-field sensitivities, η_{cw} and η_{pulsed}, are given by

$$\eta_{cw} = \frac{4}{3\sqrt{3}}\frac{h}{g_e\mu_B}\frac{\Delta\nu}{C_{cw}\sqrt{R}}, \tag{5}$$

$$\eta_{\text{pulsed}} = \frac{8}{3\sqrt{3}}\frac{\hbar}{g_e\mu_B}\frac{1}{C_{\text{pulsed}}\sqrt{Rt_R}}\frac{\sqrt{t_I + T_2^* + t_R}}{T_2^*}, \tag{6}$$

where $h(\hbar)$ is Planck's (reduced) constant, g_e is the effective g factor for Cr(o-tolyl)$_4$, μ_B is the Bohr magneton, R is the photon-detection rate, $\Delta\nu$ is the cw-ODMR linewidth, C_{pulsed}

is the pulsed ODMR contrast, t_I is the initialization pulse length, t_R is the readout pulse length, and T_2^* is the inhomogeneous dephasing time.

Using $R = 300$ counts/s, $g_e = 2$, $\Delta\nu = 42$ MHz, $T_2^* \approx 8$ ns (estimated from cw-ODMR linewidths), $t_I \approx 300$ μs, $t_R = 20$ μs, $C_{cw} \approx 10^{-3}$, and $C_{\text{pulsed}} \approx 0.03$ from previous measurements yield η_{cw} and η_{pulsed} of 67 mT Hz$^{-1/2}$ and 14 mT Hz$^{-1/2}$, respectively. The estimated sensitivities offer an upper bound on the sensitivity of individual Cr^{4+} color centers and likely can be improved for dedicated magnetic-field sensing applications. For example, the same molecular color center, Cr(*o*-tolyl)$_4$, diluted in an alternative host exhibited superior $C_{\text{pulsed}} = 0.4$ [44], which should improve η_{pulsed} to 1 mT Hz$^{-1/2}$. Moreover, these figures of merit for magnetic-field sensitivity are highly dependent on the method of measurement (e.g., Ramsey, cw, pulsed, see Ref. [43] for further details) and may be improved through extrinsic factors, such as improved collection efficiencies, Purcell enhanced emission rates, and stronger microwave drives. Thus, we present these values, along with previous demonstrations measuring magnetic fields from 0–10 mT, to suggest that Cr(*o*-tolyl)$_4$ may provide a suitable sensor to detect magnetic fields arising from CrI_3 monolayers.

Figure 3(b) shows the total magnetic field sensed as a function of distance decomposed into contributions from proximity exchange and the magnetostatics. Proximity exchange contributions are dominate up to 8 Å from CrI_3. The short span over which proximity exchange is the main contribution to the total magnetic field is due to the cubic distance dependent, d^3, decrease in proximity exchange compared with the d^{-1} decrease for direct magnetic fields.

Although our analysis utilizes a single molecular color center, experimental setups would require molecular films, which may exhibit texture and grain boundaries. Such microstructure could elicit separate responses from distortions in the geometry of the molecule, which has a large effect on the excited-state energy. This could lead to increased variance in energy changes, adding complexity to interpretation of ODMR results. These alterations to the molecule's properties could be mitigated by creating highly ordered, atomically smooth films. Past studies on transition-metal complex thin films suggest that this is challenging and motivates improvements in processing methods [45,46].

The magnetic field from CrI_3 is a vector quantity, yet these sensors will yield a scalar value for the field that is projected along the easy axis of the spin qubit (also known as the quantization axis). The axis of quantization is important in both understanding the field magnitude for our single color center model and how molecular conformations in deposited films, further from the analyte, modify the alignment of the molecule's easy axis with respect to the direction of the magnetic field, thereby altering sensitivity. To understand how these factors affect the fidelity of the field read-out, we next determined the spin-quantization axis by performing noncollinear relativistic DFT calculations with spin-orbit coupling on isolated Cr(*o*-tolyl)$_4$, Appendix C. In the reference frame of the combined molecule-substrate system [Fig. 4(d), inset], the quantization axis has the unit vector (−0.784, 0.500, 0.368). Figure 4(d) shows that the magnetic field

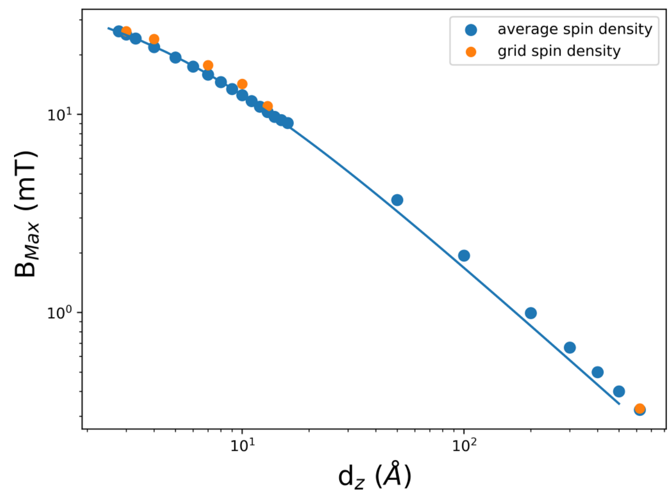

FIG. 5. Comparison of the maximum calculated magnetic fields from the average spin-density (blue) and grid spin-density (orange) methods.

decreases with d_z independent of the quantization axis, and these values are in good quantitative agreement with experiment. There is, however, a strong dependence of the field strength on the axis of quantization, e.g., the largest different being 14 mT at 2.7 Å from the substrate.

Tailoring the easy axis of the sensor to the direction of the field would allow for maximum sensitivity. We now use this approach to determine the simulated magnetic fields along the easy axis of a diamond-NV center and compare with the MCC. We find that they are within 20 μT at $d_z = 60$ nm. A comparison of the magnetic field quantized along the easy axis from the Cr(*o*-tolyl)$_4$ on CrI_3 to the field quantized along the [111] easy axis of a diamond-NV center shows the two exhibit similar field strengths with the diamond NV center slightly larger. Neither the lowest-energy orientation of Cr(*o*-tolyl)$_4$ nor the known easy axis of the NV center are aligned with the axis having the largest magnetic field for CrI_3 (the z axis). The flexibility of MCC both in the ligand and matrix may be useful variables to tune in maximizing the sensitivity of the sensor.

Cr(*o*-tolyl)$_4$ has a highly-temperature-dependent relaxation time varying from 500 to 3 μs between 5 and 40 K, respectively, which necessitates sensing at low temperatures [13,14]. Our use case for the sensor shown here, monolayer magnets, also have low ordering temperatures (45 K for CrI_3 and 42 K for $CrGeTe_3$) [47–49], making the MCC an ideal sensing platform. Other potential use cases for these sensors include Kitaev materials, a SOC-entangled subclass of Mott insulators, such as $RuCl_3$, which exhibits unique zigzag magnetic ordering below 7 K [50,51], or other complex layered 2D magnets like metal-organic frameworks [52,53]. Additionally, magnetic defects, that may harm the performance of superconducting qubits via decoherence channels, could be spatially mapped, as these magnetic defects are known to occur below 12 K [54,55]. Sensing higher-temperature phenomena will require increasing relaxation times, and there are substantial efforts focused on engineering ligand environments in molecular color centers to expand the useful temperature ranges to above liquid nitrogen [14,42,56,57].

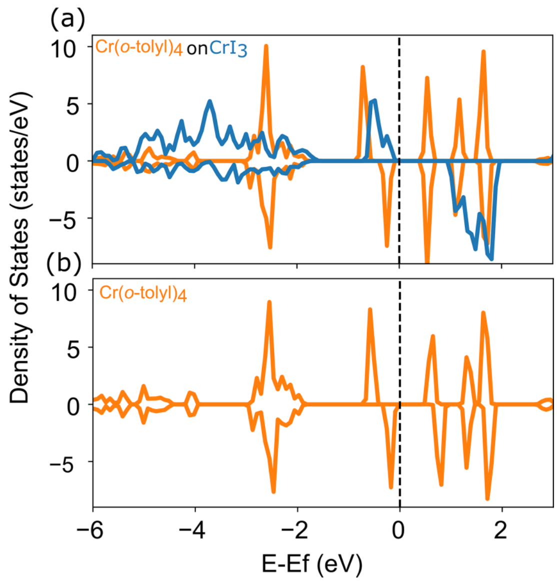

FIG. 6. Density of states for the constrained band calculation of (a) Cr(o-tolyl)$_4$ on CrI_3 and (b) isolated Cr(o-tolyl)$_4$. Both configurations show a doubly occupied Cr(o-tolyl)$_4$ orbital near the Fermi level.

IV. Conclusions. In summary, we find that magnetic fields range from 94 to 0.28 mT over 3 Å to 60 nm, respectively, from CrI_3 using a single-sensing platform. At distances beyond 8 Å from the 2D magnet, direct magnetic fields, i.e., the primary field probed by traditional magnetic-field sensors, dominates the signal over the shorter range proximity exchange interaction. Our results show how MCC can be used to sense magnetic fields with high fidelity over a range of distances and how the platform forms a novel metrology to discern phenomena in low-dimensional systems. The inherent flexibility of MCC suggest alterations to the molecule could allow for optimizing the easy axis direction and the orientation of the molecule on the surface to allow for improved sensing.

The data that support the findings of this study are available from the corresponding author upon reasonable request. Scripts for magnetostatic modeling are available online [58].

Acknowledgments. This work was supported by the U.S. Department of Energy, Office of Science, Basic Energy Sciences under Award No. DE-SC0019356. This work used resources at the National Energy Research Scientific Computing Center, a DOE Office of Science User Facility supported by the Office of Science of the U.S. Department of Energy under Contract No. DE-AC02-05CH11231 using NERSC Award No. BES-ERCAP0020980.

Appendix A: Magnetic-field calculation methods. Figure 5 compares the numerical results of the grid based calculations to those of the average spin density.

Appendix B: Adsorption site and molecular orientation effects. The orientation of the molecule for the proximity exchange calculations was selected based on our total-energy calculations. The combined system configuration with the molecule on the perpendicular and parallel orientations, Cr and hollow adsorption sites, and rotated in-plane around the z axis at 0° and 45° configurations were considered. Table I shows the results of these calculations where there are very small changes in total energy with respect to each of these parameters. The most stable structure in the perpendicular orientation, on the hollow site, and with a 0° xy plane rotation angle was used for more extensive calculations presented above.

TABLE I. Total energy per atom for Cr(o-tolyl)$_4$ adsorbed on CrI_3 with different configurations.

Orientation-rotation angle (site)	Energy per atom (μeV)
Parallel-0° (Cr)	20
Parallel-0° (hollow)	30
Perpendicular-0° (Cr)	40
Perpendicular-0° (hollow)	0
Parallel-45° (Cr)	30
Parallel-45° (hollow)	40
Perpendicular-45° (Cr)	30
Perpendicular-45° (hollow)	10

As the energy of the different configurations for Cr(o-tolyl)$_4$ on CrI_3 were very similar, we then examined changes across the ground-state electronic structures. We also found very small changes in $E_{gs}^{\uparrow\downarrow}$ and $E_{gs}^{\uparrow\uparrow} \approx 0.1$ meV (Table II). These changes are an order of magnitude smaller than those in the excited state.

Appendix C: Quantization axis calculations. To determine the quantization axis for the molecule, we performed noncollinear relativistic DFT calculations with spin-orbit coupling on isolated Cr(o-tolyl)$_4$ in two geometries: fully relaxed and as absorbed on CrI_3. To perform these calculations, we aligned the easy axis of the molecule with the [100], [010], and [001] directions and calculated the total energy and the final noncollinear magnetic moment. The results are shown in Tables III and IV for the relaxed and as adsorbed molecules, respectively. We find that regardless of the molecule's geometry that the total energy is lowest when the easy axis aligns with the [001] axis in the reference frame of the isolated molecule.

When Cr(o-tolyl)$_4$ is adsorbed on to CrI_3 the quantization axis is rotated compared with its original reference frame. In the reference frame of the combined system, the previous [001] axis is now aligned with the unit vector (−0.784, 0.500, 0.368). It is this unit vector that we use as the quantization axis for Cr(o-tolyl)$_4$ in the magnetostatic calculations.

Appendix D: Constrained band density of states. Figure 6 shows the constrained band density of states for Cr(o-tolyl)$_4$ and Cr(o-tolyl)$_4$ adsorbed on CrI_3.

TABLE II. Ground-state energies for the molecule with different orientations and adsorbed on different adsorption sites. Results are averaged across 0° and 45° rotations in the xy plane of the combined system.

Orientation (site)	$E_{gs}^{\uparrow\uparrow}$ (eV)	$E_{gs}^{\uparrow\downarrow}$ (eV)
Parallel (Cr)	1.51697	1.64336
Parallel (hollow)	1.51670	1.64397
Perpendicular (Cr)	1.51651	1.64392
Perpendicular (hollow)	1.51681	1.64362

TABLE III. Total energy and vector magnetic moments from DFT on relaxed Cr(o-tolyl)$_4$.

Axis	E (μeV)	M_x (μ_B)	M_y (μ_B)	M_z (μ_B)
[100]	3.86	2.00	0.00	0.00
[010]	4.00	0.00	2.00	0.00
[001]	0.00	0.00	0.00	2.00

TABLE IV. Total energy and vector magnetic moments from DFT on as adsorbed Cr(o-tolyl)$_4$.

Axis	E (μeV)	M_x (μ_B)	M_y (μ_B)	M_z (μ_B)
[100]	0.30	2.00	0	0
[010]	8.00	−0.01	2.00	0.01
[001]	0.00	0	0	2.00

[1] M. J. H. Ku, T. X. Zhou, Q. Li, Y. J. Shin, J. K. Shi, C. Burch, L. E. Anderson, A. T. Pierce, Y. Xie, A. Hamo, U. Vool, H. Zhang, F. Casola, T. Taniguchi, K. Watanabe, M. M. Fogler, P. Kim, A. Yacoby, and R. L. Walsworth, Imaging viscous flow of the Dirac fluid in graphene, Nature (London) **583**, 537 (2020).

[2] U. Vool, A. Hamo, G. Varnavides, Y. Wang, T. X. Zhou, N. Kumar, Y. Dovzhenko, Z. Qiu, C. A. C. Garcia, A. T. Pierce, J. Gooth, P. Anikeeva, C. Felser, P. Narang, and A. Yacoby, Imaging phonon-mediated hydrodynamic flow in WTe_2, Nat. Phys. **17**, 1216 (2021).

[3] E. Marchiori, L. Ceccarelli, N. Rossi, L. Lorenzelli, C. L. Degen, and M. Poggio, Nanoscale magnetic field imaging for 2D materials, Nat. Rev. Phys. **4**, 49 (2022).

[4] P. Ripka, New directions in fluxgate sensors, J. Magn. Magn. Mater. **215**, 735 (2000).

[5] Y. Zheng, L. Huang, Z. Zhang, J. Jiang, K. Wang, L.-M. Peng, and G. Yu, Sensitivity enhancement of graphene Hall sensors modified by single-molecule magnets at room temperature, RSC Adv. **7**, 1776 (2017).

[6] R. Li, S. Zhang, S. Luo, Z. Guo, Y. Xu, J. Ouyang, M. Song, Q. Zou, L. Xi, X. Yang, J. Hong, and L. You, A spin–orbit torque device for sensing three-dimensional magnetic fields, Nat. Electron. **4**, 179 (2021).

[7] J. M. Taylor, P. Cappellaro, L. Childress, L. Jiang, D. Budker, P. R. Hemmer, A. Yacoby, R. Walsworth, and M. D. Lukin, High-sensitivity diamond magnetometer with nanoscale resolution, Nat. Phys. **4**, 810 (2008).

[8] C. L. Degen, F. Reinhard, and P. Cappellaro, Quantum sensing, Rev. Mod. Phys. **89**, 035002 (2017).

[9] S. Hong, M. S. Grinolds, L. M. Pham, D. Le Sage, L. Luan, R. L. Walsworth, and A. Yacoby, Nanoscale magnetometry with NV centers in diamond, MRS Bull. **38**, 155 (2013).

[10] M. Radtke, E. Bernardi, A. Slablab, R. Nelz, and E. Neu, Nanoscale sensing based on nitrogen vacancy centers in single crystal diamond and nanodiamonds: Achievements and challenges, Nano Futures **3**, 042004 (2019).

[11] M. Xie, X. Yu, L. V. H. Rodgers, D. Xu, I. Chi-Durán, A. Toros, N. Quack, N. P. de Leon, and P. C. Maurer, Biocompatible surface functionalization architecture for a diamond quantum sensor, Proc. Natl. Acad. Sci. USA **119**, e2114186119 (2022).

[12] L. Tesi, F. Stemmler, M. Winkler, S. S. Y. Liu, S. Das, X. Sun, M. Zharnikov, S. Ludwigs, and J. van Slageren, Modular approach to creating functionalized surface arrays of molecular qubits, Adv. Mater. **35**, 2208998 (2023).

[13] S. L. Bayliss, D. W. Laorenza, P. J. Mintun, B. D. Kovos, D. E. Freedman, and D. D. Awschalom, Optically addressable molecular spins for quantum information processing, Science **370**, 1309 (2020).

[14] D. W. Laorenza, A. Kairalapova, S. L. Bayliss, T. Goldzak, S. M. Greene, L. R. Weiss, P. Deb, P. J. Mintun, K. A. Collins, D. D. Awschalom, T. C. Berkelbach, and D. E. Freedman, Tunable Cr^{4+} molecular color centers, J. Am. Chem. Soc. **143**, 21350 (2021).

[15] W. F. Koehl, B. Diler, S. J. Whiteley, A. Bourassa, N. T. Son, E. Janzén, and D. D. Awschalom, Resonant optical spectroscopy and coherent control of Cr^{4+} spin ensembles in SiC and GaN, Phys. Rev. B **95**, 035207 (2017).

[16] B. Diler, S. J. Whiteley, C. P. Anderson, G. Wolfowicz, M. E. Wesson, E. S. Bielejec, F. Joseph Heremans, and D. D. Awschalom, Coherent control and high-fidelity readout of chromium ions in commercial silicon carbide, npj Quantum Inf. **6**, 11 (2020).

[17] J. R. Maze, P. L. Stanwix, J. S. Hodges, S. Hong, J. M. Taylor, P. Cappellaro, L. Jiang, M. V. G. Dutt, E. Togan, A. S. Zibrov, A. Yacoby, R. L. Walsworth, and M. D. Lukin, Nanoscale magnetic sensing with an individual electronic spin in diamond, Nature (London) **455**, 644 (2008).

[18] L. Rondin, J.-P. Tetienne, P. Spinicelli, C. Dal Savio, K. Karrai, G. Dantelle, A. Thiaville, S. Rohart, J.-F. Roch, and V. Jacques, Nanoscale magnetic field mapping with a single spin scanning probe magnetometer, Appl. Phys. Lett. **100**, 153118 (2012).

[19] A. Kubica, J. Kowalewski, D. Kruk, and M. Odelius, Zero-field splitting in nickel(II) complexes: A comparison of DFT and multi-configurational wavefunction calculations, J. Chem. Phys. **138**, 064304 (2013).

[20] M. Gibertini, M. Koperski, A. F. Morpurgo, and K. S. Novoselov, Magnetic 2D materials and heterostructures, Nat. Nanotechnol. **14**, 408 (2019).

[21] Q. H. Wang, A. Bedoya-Pinto, M. Blei, A. H. Dismukes, A. Hamo, S. Jenkins, M. Koperski, Y. Liu, Q.-C. Sun, E. J. Telford, H. H. Kim, M. Augustin, U. Vool, J.-X. Yin, L. H. Li, A. Falin, C. R. Dean, F. Casanova, R. F. L. Evans, M. Chshiev *et al.*, The magnetic genome of two-dimensional van der Waals materials, ACS Nano **16**, 6960 (2022).

[22] D. Zhong, K. L. Seyler, X. Linpeng, R. Cheng, N. Sivadas, B. Huang, E. Schmidgall, T. Taniguchi, K. Watanabe, M. A. McGuire, W. Yao, D. Xiao, K.-M. C. Fu, and X. Xu, Van der Waals engineering of ferromagnetic semiconductor heterostructures for spin and valleytronics, Sci. Adv. **3**, e1603113 (2017).

[23] L. Thiel, Z. Wang, M. A. Tschudin, D. Rohner, I. Gutiérrez-Lezama, N. Ubrig, M. Gibertini, E. Giannini, A. F. Morpurgo, and P. Maletinsky, Probing magnetism in 2D materials at the nanoscale with single-spin microscopy, Science **364**, 973 (2019).

[24] K. Zollner, P. E. Faria Junior, and J. Fabian, Giant proximity exchange and valley splitting in transition metal

dichalcogenide/hBN/(Co, Ni) heterostructures, Phys. Rev. B **101**, 085112 (2020).

[25] K. Zollner, P. E. Faria Junior, and J. Fabian, Proximity exchange effects in $MoSe_2$ and WSe_2 heterostructures with CrI_3: Twist angle, layer, and gate dependence, Phys. Rev. B **100**, 085128 (2019).

[26] E. C. Ahn, 2D materials for spintronic devices, npj 2D Mater. Appl. **4**, 17 (2020).

[27] K. Zollner and J. Fabian, Proximity effects in graphene on monolayers of transition-metal phosphorus trichalcogenides MPX_3(M : Mn, Fe, Ni, Co, and X : S, Se), Phys. Rev. B **106**, 035137 (2022).

[28] G. Kresse and J. Hafner, *Ab initio* molecular dynamics for liquid metals, Phys. Rev. B **47**, 558 (1993).

[29] G. Kresse and J. Hafner, *Ab initio* molecular-dynamics simulation of the liquid-metal–amorphous-semiconductor transition in germanium, Phys. Rev. B **49**, 14251 (1994).

[30] G. Kresse and J. Furthmüller, Efficiency of ab-initio total energy calculations for metals and semiconductors using a plane-wave basis set, Comput. Mater. Sci. **6**, 15 (1996).

[31] G. Kresse and J. Furthmüller, Efficient iterative schemes for *ab initio* total-energy calculations using a plane-wave basis set, Phys. Rev. B **54**, 11169 (1996).

[32] G. Kresse and D. Joubert, From ultrasoft pseudopotentials to the projector augmented-wave method, Phys. Rev. B **59**, 1758 (1999).

[33] P. E. Blöchl, Projector augmented-wave method, Phys. Rev. B **50**, 17953 (1994).

[34] J. P. Perdew, K. Burke, and M. Ernzerhof, Generalized gradient approximation made simple [Phys. Rev. Lett. **77**, 3865 (1996)], Phys. Rev. Lett. **78**, 1396 (1997).

[35] J. P. Perdew, K. Burke, and M. Ernzerhof, Generalized gradient approximation made simple, Phys. Rev. Lett. **77**, 3865 (1996).

[36] A. Hellman, B. Razaznejad, and B. I. Lundqvist, Potential-energy surfaces for excited states in extended systems, J. Chem. Phys. **120**, 4593 (2004).

[37] J. Gavnholt, T. Olsen, M. Engelund, and J. Schiøtz, Δ self-consistent field method to obtain potential energy surfaces of excited molecules on surfaces, Phys. Rev. B **78**, 075441 (2008).

[38] D. Wang and B. Sanyal, Systematic study of monolayer to trilayer CrI_3: Stacking sequence dependence of electronic structure and magnetism, J. Phys. Chem. C **125**, 18467 (2021).

[39] S. Grimme, J. Antony, S. Ehrlich, and H. Krieg, A consistent and accurate *ab initio* parametrization of density functional dispersion correction (DFT-D) for the 94 elements H-Pu, J. Chem. Phys. **132**, 154104 (2010).

[40] S. Grimme, S. Ehrlich, and L. Goerigk, Effect of the damping function in dispersion corrected density functional theory, J. Comput. Chem. **32**, 1456 (2011).

[41] A. Okuniewski, D. Rosiak, J. Chojnacki, and B. Becker, Coordination polymers and molecular structures among complexes of mercury(II) halides with selected 1-benzoylthioureas, Polyhedron **90**, 47 (2015).

[42] M. J. Amdur, K. R. Mullin, M. J. Waters, D. Puggioni, M. K. Wojnar, M. Gu, L. Sun, P. H. Oyala, J. M. Rondinelli, and D. E. Freedman, Chemical control of spin-lattice relaxation to discover a room temperature molecular qubit, Chem. Sci. **13**, 7034 (2022).

[43] J. F. Barry, J. M. Schloss, E. Bauch, M. J. Turner, C. A. Hart, L. M. Pham, and R. L. Walsworth, Sensitivity optimization for NV-diamond magnetometry, Rev. Mod. Phys. **92**, 015004 (2020).

[44] S. L. Bayliss, P. Deb, D. W. Laorenza, M. Onizhuk, G. Galli, D. E. Freedman, and D. D. Awschalom, Enhancing spin coherence in optically addressable molecular qubits through host-matrix control, Phys. Rev. X **12**, 031028 (2022).

[45] K. Xiao, W. Deng, J. K. Keum, M. Yoon, I. V. Vlassiouk, K. W. Clark, A.-P. Li, I. I. Kravchenko, G. Gu, E. A. Payzant, B. G. Sumpter, S. C. Smith, J. F. Browning, and D. B. Geohegan, Surface-induced orientation control of CuPc molecules for the epitaxial growth of highly ordered organic crystals on graphene, J. Am. Chem. Soc. **135**, 3680 (2013).

[46] M. Stöhr, M. Gabriel, and R. Möller, Investigation of the growth of PTCDA on Cu(110): An STM study, Surf. Sci. **507-510**, 330 (2002).

[47] S. Tiwari, M. L. Van de Put, B. Sorée, and W. G. Vandenberghe, Magnetic order and critical temperature of substitutionally doped transition metal dichalcogenide monolayers, npj 2D Mater. Appl. **5**, 54 (2021).

[48] K. S. Burch, D. Mandrus, and J.-G. Park, Magnetism in two-dimensional van der Waals materials, Nature (London) **563**, 47 (2018).

[49] A. B. Georgescu, A. J. Millis, and J. M. Rondinelli, Trigonal symmetry breaking and its electronic effects in the two-dimensional dihalides MX_2 and trihalides MX_3, Phys. Rev. B **105**, 245153 (2022).

[50] S. Trebst and C. Hickey, Kitaev materials, Phys. Rep. **950**, 1 (2022).

[51] J. A. Sears, M. Songvilay, K. W. Plumb, J. P. Clancy, Y. Qiu, Y. Zhao, D. Parshall, and Y.-J. Kim, Magnetic order in α-$RuCl_3$: A honeycomb-lattice quantum magnet with strong spin-orbit coupling, Phys. Rev. B **91**, 144420 (2015).

[52] Y. Wang, M. E. Ziebel, L. Sun, J. T. Gish, T. J. Pearson, X.-Z. Lu, A. E. Thorarinsdottir, M. C. Hersam, J. R. Long, D. E. Freedman, J. M. Rondinelli, D. Puggioni, and T. D. Harris, Strong magnetocrystalline anisotropy arising from metal–ligand covalency in a metal–organic candidate for 2D magnetic order, Chem. Mater. **33**, 8712 (2021).

[53] A. E. Thorarinsdottir and T. D. Harris, Metal–organic framework magnets, Chem. Rev. (Washington, DC, US) **120**, 8716 (2020).

[54] C. M. Fang, M. A. van Huis, Q. Xu, R. J. Cava, and H. W. Zandbergen, Unexpected origin of magnetism in monoclinic $Nb_{12}O_{29}$ from first-principles calculations, J. Mater. Chem. C **3**, 651 (2015).

[55] E. Sheridan, T. F. Harrelson, E. Sivonxay, K. A. Persson, M. V. P. Altoé, I. Siddiqi, D. F. Ogletree, D. I. Santiago, and S. M. Griffin, Microscopic theory of magnetic disorder-induced decoherence in superconducting Nb films, arXiv:2111.11684.

[56] A. J. Fielding, S. Fox, G. L. Millhauser, M. Chattopadhyay, P. M. Kroneck, G. Fritz, G. R. Eaton, and S. S. Eaton, Electron spin relaxation of copper(II) complexes in glassy solution between 10 and 120 K, J. Magn. Reson. **179**, 92 (2006).

[57] M. Atzori, S. Benci, E. Morra, L. Tesi, M. Chiesa, R. Torre, L. Sorace, and R. Sessoli, Structural effects on the spin dynamics of potential molecular qubits, Inorg. Chem. (Washington, DC, US) **57**, 731 (2018).

[58] https://github.com/MTD-group/Magnetostatic-Model-CrI3.